A&A 518, A15 (2010)
DOI: 10.1051/0004-6361/200913070

Astronomy & Astrophysics

Near-infrared properties of metal-poor globular clusters in the Galactic bulge direction⋆

S.-H. Chun[1], J.-W. Kim[2], I.-G. Shin[1], C. Chung[1], D.-W. Lim[1], J.-H. Park[3], H.-I. Kim[3], W. Han[3], and Y.-J. Sohn[1,3]

[1] Department of Astronomy, Yonsei University, 120-749 Seoul, Korea
e-mail: sohnyj@yonsei.ac.kr; shchun@galaxy.yonsei.ac.kr
[2] Institute for Computational Cosmology, Department of Physics, Durham University, South Road, Durham DH1 3LE, UK
[3] Korea Astronomy and Space Science Institute, 305-348 Daejeon, Korea

Received 5 August 2009 / Accepted 16 April 2010

ABSTRACT

Aims. J, H, and K' images obtained from the near-infrared imager CFHTIR on the Canada-France-Hawaii Telescope are used to derive the morphological parameters of the red giant branch (RGB) in the near-infrared color-magnitude diagrams for 12 metal-poor globular clusters in the Galactic bulge direction. Using the compiled data set of the RGB parameters for the observed 12 clusters, in addition to the previously studied 5 clusters, we discuss the properties of the RGB morphology for the clusters and compare them with the calibration relations for the metal-rich bulge clusters and the metal-poor halo clusters.

Methods. The photometric RGB shape indices, such as colors at fixed magnitudes of $M_K = M_H = (-5.5, -5, -4,$ and $-3)$, magnitudes at fixed colors of $(J-K)_o = (J-H)_o = 0.7$, and the RGB slope, were measured from the fiducial normal points defined in the near-infrared color–magnitude diagrams for each cluster. The magnitudes of RGB bump and tip were also estimated from the differential and cumulative luminosity functions of the selected RGB stars. The derived RGB parameters were used to examine the overall behaviors of the RGB morphology as a function of cluster metallicity.

Results. The correlations between the near-infrared photometric RGB shape indices and the cluster metallicity for the program clusters compare favorably with the previous observational calibration relations for metal-rich clusters in the Galactic bulge and the metal-poor halo clusters. The observed near-infrared magnitudes of the RGB bump and tip for the investigated clusters also accord with the previous calibration relations for the Galactic bulge clusters.

Key words. Galaxy: structure – globular clusters: general – stars: evolution – infrared: stars – techniques: photometric

1. Introduction

The current view of the Galaxy formation is mainly focused on the hierarchical merging paradigm in the cold dark matter cosmology. As tracers of the early formation and the current structure of the Galaxy, globular clusters play a key role in studies of the paradigm, because they are present from the central bulge to the outer halo with various metallicities. Particularly, the Galactic bulge harbors a globular cluster population with a broad metallicity distribution that extends from about twice solar to less than one-tenth solar abundance (Ortolani 1999), while most field stars in the bulge have near-solar metallicity (McWilliam & Rich 1994; Zoccali et al. 2003).

The metal-rich globular clusters in the the Galactic bulge share the kinematics, spatial distribution, and composition of the bulge field stars (e.g., Minniti & Zoccali 2008, and references therin). This indicates that metal-rich globular clusters are associated with the Galactic bulge, which is recognized as the dominant proto-Galactic building block (e.g., Côté et al. 2000). On the other hand, the origin of the metal-poor globular clusters in the Galactic bulge direction is still a subject of debate since accurate measurements of kinematics and high-resolution chemical abundances are lacking. In the hierarchical model of the Galaxy formation, however, old metal-poor field stars in the bulge form via merging and accretion events in the early Universe (Nakasato & Nomoto 2003). In this sense, the metal-poor clusters currently located in the central region of the Galaxy might be the oldest objects, which did not originally form in the Galactic bulge. Thus, the metal-poor clusters in the bulge region can play a key role in understanding the early epoch of the formation of the Galactic bulge.

In the Milky Way, about 150 globular clusters are listed in the database of Harris (1996), which was revised in 2003. Recently, new faint clusters and cluster candidates have also been found (e.g., Carraro 2005; Kobulnicky et al. 2005; Willman et al. 2005; Froebrich et al. 2007). Out of 43 globular clusters located within 3 kpc of the Galactic center (Harris 1996), 22 are metal-poor ([Fe/H] < -1.0) and 21 are metal-rich ([Fe/H] > -1.0). Recently, Valenti et al. (2007) has presented near-infrared, color-magnitude diagrams (CMDs) and physical parameters for a sample of 24 globular clusters toward the Galactic bulge and located within $|b| \leqq 10°$ and $|l| \leqq 20°$. They discuss the near-infrared properties of the red giant branch (RGB) for 12 observed clusters, in addition to those previously studied by their group (e.g., Ferraro et al. 2000; Valenti et al. 2004a,b,c, 2005; Origlia et al. 2005). However, their sample of the clusters strongly favor the metal-rich population; i.e., 17 out of the 24 are relatively metal-rich with [Fe/H] > -1.0, taking a bulge origin into account for the metal-rich globular clusters.

⋆ Based on observations carried out at the Canada-France-Hawaii Telescope, operated by the National Research Council of Canada, the Centre National de la Recherche Scientifique de France, and the University of Hawaii. This is a part of the survey for the Galactic bulge clusters using the CFHT, organized by the Korea Astronomy and Space Science Institute.

In our research, we have focused on obtaining a moderately deep, homogeneous photometric data set in the near-infrared regime for the metal-poor clusters in the bulge direction. Near-infrared photometry offers advantages for studying the cool population of the RGB stars in the Galactic globular clusters, because of its high sensitivity to low temperature. In addition, high extinctions toward the bulge can be reduced by observing the near-infrared wavelengths, as the extinction in the K band is only ∼10 percent of that in the V band (Rieke & Lebofsky 1985). Using these bases, Kim et al. (2006) presented the morphological properties of the RGB in the near-infrared CMDs for five metal-poor clusters of the Galactic bulge (NGC 6541, NGC 6642, NGC 6681, NGC 6717, and NGC 6723) and also for three halo clusters.

In this paper, we report new results of the near-infrared photometry for 12 metal-poor clusters and present a homogeneous photometric data set of the RGB morphology for 17 globular clusters, covering ∼75% of the total 22 metal-poor globular clusters in the Galactic bulge direction. The results of the RGB morphology for the program clusters are compared with the previously published calibrations of Valenti et al. (2004a,b, 2007). The observations, procedures for data reduction, and phtometric measurements are described in Sect. 2. In Sect. 3, we describe the near-infrared CMDs and the fiducial normal points of target clusters. In Sect. 4, the morphological properties of CMDs, such as RGB shape feature, RGB bump, and RGB tip, are presented. Finally, the results are discussed and summarized in Sect. 5.

2. Observations, data reduction, and photometric measurements

Observations were obtained during the nights of June 1, 2002, and April 20-21, 2003. Using the CFHTIR imager mounted on the f/8 Cassegrain focus of the Canada-France-Hawaii telescope (CFHT), the fields centered on each cluster were observed with J, H, and K' filters. The CFHTIR contains a 1024 × 1024 Hg:Cd:Te array. Its angular scale is 0.211″/pixel, so that each image covers a total field-of-view of 3.6′ × 3.6′. The observations were split into short and long exposures for each filter in order to optimize the photometry of bright and faint stars. The images by short and long exposures are combinations of four 1-s or 2-s exposures, and of eight 30-s exposures, respectively. A four-point square dither pattern was used to identify and then reject bad pixels and cosmic rays in the observed images. In both runs, the UKIRT standard stars and M13 were also observed for a photometric standardization. The summary of observations for the target clusters is presented in Table 1.

Calibration frames of darks, flats, and blank-sky backgrounds were also obtained during the runs. Dark frames were recorded at the beginning and the end of each run. Dome flats were made by subtracting exposures of the dome white spot taken with the lamps off from those taken with the lamps on. Thermal emission patterns were constructed by combining flat-fielded images of blank sky regions.

The process of data reduction consists of subtracting a dark frame, dividing by the normalized flat image for each filter, and subtracting the thermal signature and the sky background level estimated by the mode of pixel intensity distribution. Then, the processed images were combined for each exposure after aligning the dither offsets. The seeing conditions of the reduced images range between 0.″6 ∼ 0.″9.

The brightness of stars in the clusters was measured with the point-spread function fitting routine DAOPHOT II/ALLSTAR (Stetson 1987; Stetson & Harris 1988). The brightness of stars around the RGB tip was measured only in short-exposure images because of saturation in long-exposure images, while faint stars were detected only in long-exposure images. For stars detected in both short and long exposures, measurements with smaller photometric error were assigned to the brightness. To avoid false detection, only stars detected in all filters with detection errors of less than 0.2 mag were considered for the photometric analysis. The photometric calibration equations obtained from UKIRT standard stars were then applied to the magnitudes of the stars on the target clusters. Standardizations were also double-checked in direct star-to-star comparison with the photometry of bright stars in M13 of Kim et al. (2006). As shown in Kim et al. (2006), there are only small photometric offsets, $\triangle K = 0.03 \pm 0.01$ and $\triangle (J-K) = 0.04 \pm 0.01$, between the photometric data with the UKIRT system and those with the 2MASS system of Valenti et al. (2004c). The offsets will become negligible after the transformation of the fiducial normal points for the observed near-infrared CMD into the 2MASS photometric system (see Sect. 3). Here, we also note that the measured photometric data in the southwest quarter part of the images for the runs of 2002, and those in the southeast quarter part of the images for the runs of 2003 were not used for the subsequent photometric analyses, because of possible readout anomalies of the CFHTIR imager during the runs.

Table 1. Observational log of the target clusters.

Target	Filter	Exp. time (s)	*FWHM*(″)	Year
NGC 6333	J	4 × 1, 8 × 30	0.60, 0.67	2002
	H	4 × 1, 8 × 30	0.61, 0.58	
	K'	4 × 1, 8 × 30	0.58, 0.61	
NGC 6626	J	4 × 1, 8 × 30	0.67, 0.62	2002
	H	4 × 1, 8 × 30	0.57, 0.65	
	K'	4 × 1, 8 × 30	0.62, 0.65	
NGC 6235	J	4 × 2, 8 × 30	0.73, 0.74	2003
	H	4 × 2, 8 × 30	0.77, 0.81	
	K'	4 × 2, 8 × 30	0.72, 0.77	
NGC 6266	J	4 × 2, 8 × 30	0.82, 0.93	2003
	H	4 × 2, 8 × 30	0.73, 0.88	
	K'	4 × 2, 8 × 30	0.77, 0.92	
NGC 6273	J	4 × 2, 8 × 30	0.86, 0.87	2003
	H	4 × 2, 8 × 30	0.83, 0.74	
	K'	4 × 2, 8 × 30	0.83, 0.74	
NGC 6287	J	4 × 2, 8 × 30	0.61, 0.76	2003
	H	4 × 2, 8 × 30	0.62, 0.73	
	K'	4 × 2, 8 × 30	0.65, 0.73	
NGC 6293	J	4 × 2, 8 × 30	0.89, 1.18	2003
	H	4 × 2, 8 × 30	0.95, 0.87	
	K'	4 × 2, 8 × 30	0.66, 0.73	
NGC 6325	J	4 × 2, 8 × 30	0.73, 0.77	2003
	H	4 × 2, 8 × 30	0.65, 0.78	
	K'	4 × 2, 8 × 30	0.68, 0.73	
NGC 6355	J	4 × 2, 8 × 30	0.74, 0.80	2003
	H	4 × 2, 8 × 30	0.73, 0.87	
	K'	4 × 2, 8 × 30	0.73, 0.83	
NGC 6401	J	4 × 2, 8 × 30	0.66, 0.68	2003
	H	4 × 2, 8 × 30	0.61, 0.72	
	K'	4 × 2, 8 × 30	0.60, 0.72	
NGC 6558	J	4 × 2, 8 × 30	0.95, 0.99	2003
	H	4 × 2, 8 × 30	0.80, 0.99	
	K'	4 × 2, 8 × 30	0.73, 0.89	
Terzan 4	J	4 × 1, 8 × 30	0.68, 0.75	2003
	H	4 × 1, 8 × 30	0.65, 0.73	
	K'	4 × 1, 8 × 30	0.80, 0.72	

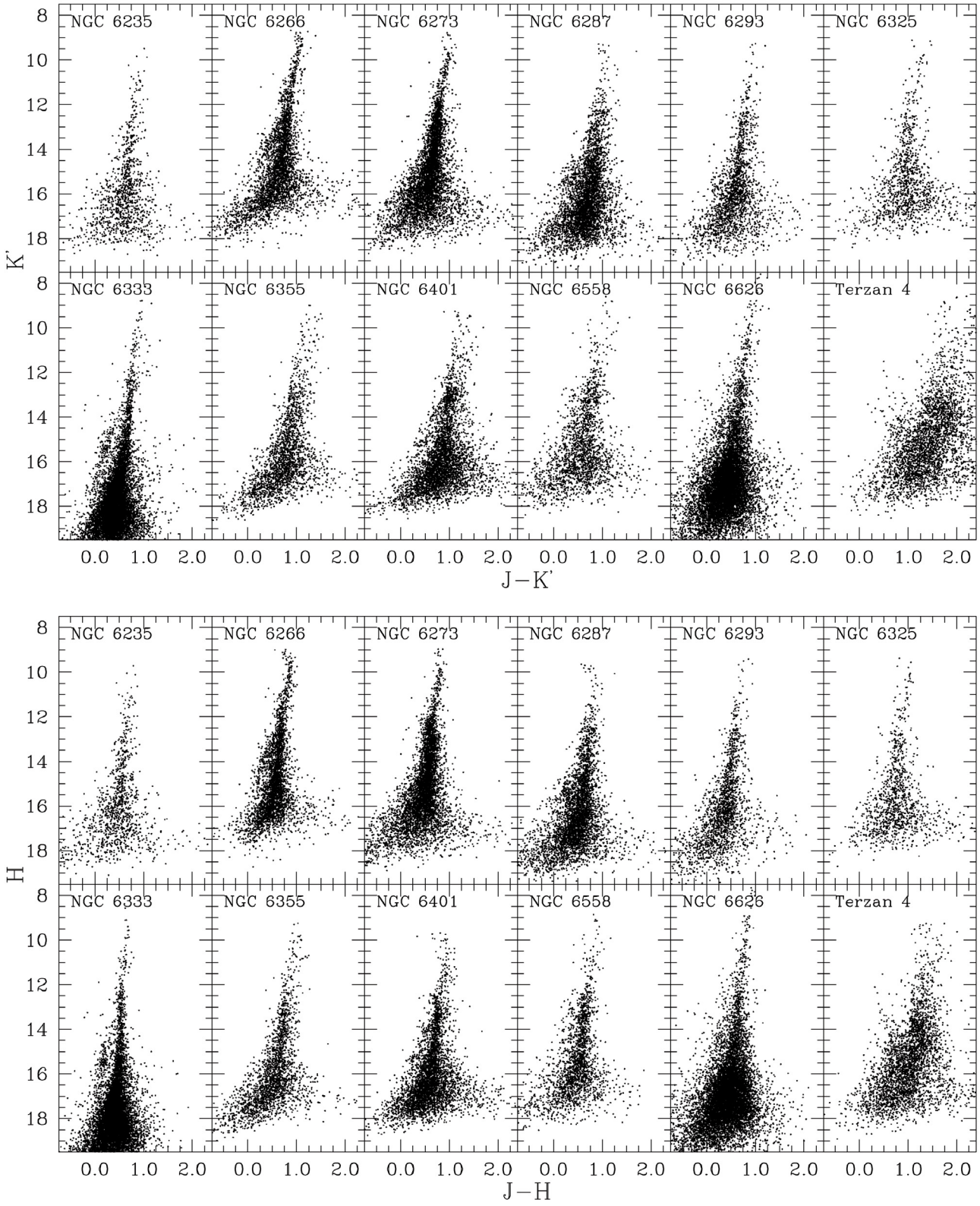

Fig. 1. The upper and lower panels are $(J - K', K')$ and $(J - H, H)$ CMDs of the observed 12 clusters.

3. Color–magnitude diagrams and fiducial normal points

Figure 1 shows $(J-K', K')$ and $(J-H, H)$ CMDs of the resolved stars in the observed area for the clusters investigated in this study. As can be seen, all of the observations are deep enough to reach the base of the RGB at $\Delta K' \sim \Delta H \approx 8$ mag fainter than the RGB tip. As we expected in the near-infrared CMDs for metal-poor globular clusters, the horizontal branch (HB) sequences are aslant compared to the RGB sequences. Scattering in the near-infrared CMDs of the target clusters might be due to both photometric errors and contamination by foreground field stars toward the Galactic bulge. It is apparent that the highly reddened tiny cluser Terzan 4 with the tidal radius $7.6' \pm 1.3'$ and

Table 2. Metallicity, distance modulus, reddening, and extinction values of the observed 12 globular clusters in the Galactic bulge.

Target	$[Fe/H]_{CG97}$	[M/H]	μ_o	$E(B-V)$	A_J	A_H	A_K
NGC 6235	−1.17	−0.97	15.05	0.36	0.325	0.207	0.132
NGC 6266	−1.08	−0.87	14.26	0.47	0.424	0.271	0.172
NGC 6273	−1.45	−1.24	14.58	0.41	0.370	0.236	0.150
NGC 6287	−1.90	−1.68	15.61	0.60	0.541	0.346	0.220
NGC 6293	−1.73	−1.53	14.79	0.41	0.370	0.236	0.150
NGC 6325	−1.21	−0.99	14.10	0.89	0.803	0.513	0.327
NGC 6333	−1.56	−1.36	14.67	0.38	0.343	0.219	0.139
NGC 6355	−1.26	−1.07	14.60	0.75	0.677	0.432	0.275
NGC 6401	−0.97	−0.74	14.61	0.72	0.649	0.415	0.264
NGC 6558	−1.21	−0.99	14.30	0.44	0.397	0.253	0.161
NGC 6626	−1.21	−0.99	13.60	0.40	0.361	0.230	0.147
Terzan 4	−1.62	−1.41	15.10	2.06	1.858	1.187	0.756

the concentration parameter $c = 0.9 \pm 0.2$ (Bonatto & Bica 2008) contain significant noise owing to strong field star contamination in the observed field.

To examine the relationship between the RGB morphological parameters in CMDs of the absolute plane and cluster's metallicity, the values of metallicity, reddening, and distance modulus were estimated for each cluster using the method adopted in Kim et al. (2006). Metallicities for target clusters are used in the Carreta & Gratton (1997) scale, $[Fe/H]_{CG97}$, to directly compare the photometric properties of the measured RGB morphology with the results presented in Valenti et al. (2004a, 2007). Metallicities $[Fe/H]_{CG97}$ of two clusters NGC 6266 and NGC 6333 were adopted from Ferraro et al. (1999). For the other clusters, we obtained $[Fe/H]_{CG97}$ by transforming the data given in Zinn (1985) into the scale of Carreta & Gratton (1997) as per Valenti et al. (2004a). We assigned $[Fe/H]_{CG97} = -1.62 \pm 0.08$ to Terzan 4, for which Stephens & Frogel (2004) measured the metallicity of 7 stars in the cluster. We also estimated global metallicities [M/H] of the target clusters by using the equation for the α elements' enhanced theoretical evolutionary sequence (Salaris et al. 1993), i.e., $[M/H] = [Fe/H]_{CG97} + \log(0.638 f_\alpha + 0.362)$ with $f_\alpha = 10^{0.30}$, where f_α is the enhancement factor of the α elements. The determined metallicity values of $[Fe/H]_{CG97}$ and [M/H] for each cluster are listed in Table 2.

Distance moduli of two clusters NGC 6266 and NGC 6333 were adopted from Ferraro et al. (1999), in which a new methodology is presented to derive distance moduli of globular clusters by matching the observed visual magnitude of the zero-age HB (V_{ZAHB}) and the theoretical synthetic HB models. For the ten other clusters, a similar procedure to that of Ferraro et al. (1999) was applied to determine the distance moduli from the synthetic and observed ZAHB levels. Synthetic HBs for each cluster with different metallicities were generated by the method used in Lee et al. (1994) with the HB evolutionary tracks of Yi et al. (1997). The details of the generated synthetic HBs with various metallicities are described in Kim et al. (2006). The synthetic HBs in the absolute plane were transformed into the observed HBs in the CMDs of the target clusters from Rich et al. (1998) for NGC 6558, Ortolani et al. (1997) for Terzan 4, and Piotto et al. (2002) for the eight other clusters. The extinction correction was calculated by using the latest compilation of $E(B-V)$ in Harris (1996) and by applying the reddening ratios of Schlegel et al. (1998). The distance modulus for each cluster was then estimated by measuring the ZAHB levels in the synthetic and observed CMDs of HB stars, taking the extinction values into account for each cluster. We determined the reddening $E(B-V) = 2.06$ for the highly reddened cluster Terzan 4 from the synthetic and observed CMDs of HB stars. This seems to be slightly less than $E(B-V) = 2.35$ in Harris (1996) and $E(B-V) = 2.31$ in Ortolani et al. (1997), but comparable to the reddening value $E(B-V) = 2.05$ of Valenti et al. (2010). The determined distance moduli μ_o for the target clusters are listed in Table 2 with reddening $E(B-V)$ and extinction values A_J, A_H, and A_K in the near-infrared wavelengths.

Prior to deriving the morphological parameters of the RGB sequence, we obtained the RGB fiducial normal points for the near-infrared CMDs of the sample clusters, following the same strategy as in Kim et al. (2006). As shown in Fig. 1, the CMD of Terzan 4 shows a significant field star contamination. In order to minimize field star contamination of the tiny cluster Terzan 4, we determined the fiducial normal points of the RGB with stars only within 16″ of the cluster center. Valenti et al. (2010) have derived the RGB ridge line of Terzan 4 using stars within 40″ of the cluster center to derive the morphological parameters. For the other clusters, the resolved stars within 30″ from the cluster center were used to construct the fiducial normal points of the RGB. We first determined the mean magnitude and color in the 0.25 mag bin of the CMDs, excluding asymptotic giant branch stars, slanted HB stars, and highly scattered foreground stars. Subsequently, we rejected stars with colors over $\pm 2\sigma$ of the mean, and the mean values of the magnitude and color were calculated again in the assigned magnitude bin. The procedure with a 2σ rejection criterion was repeated until the mean values of the magnitude and color were stable at constant values. This iterative process statistically removed the asymptotic giant branch stars, HB stars, and field stars from the RGB stars in the obtained near-infrared CMDs for the central region of the target clusters. Then, the cluster reddening and distance were used to convert the determined fiducial normal points into the absolute plane. Finally, the color and magnitude of the fiducial normal points in the UKIRT system were transformed into the 2MASS system by using Eqs. (37)–(39) from Carpenter (2001) to compare the results directly with those of Valenti et al. (2004a, 2007). Figure 2 shows the fiducial normal points in $(J-K)_o - M_K$ and $(J-H)_o - M_H$ planes for the target clusters. For bright stars saturated around the RGB tip, we estimated the fiducial normal points from the 2MASS catalog data of the area observed in this study.

4. Morphology of the near-infrared CMDs

In this section, we present and discuss the morphological properties of the near-infrared CMDs for the program clusters. The near-infrared RGB morphology for each cluster is characterized by parameters of the RGB location in colors at fixed magnitudes and in magnitudes at fixed colors, the slopes of the RGB,

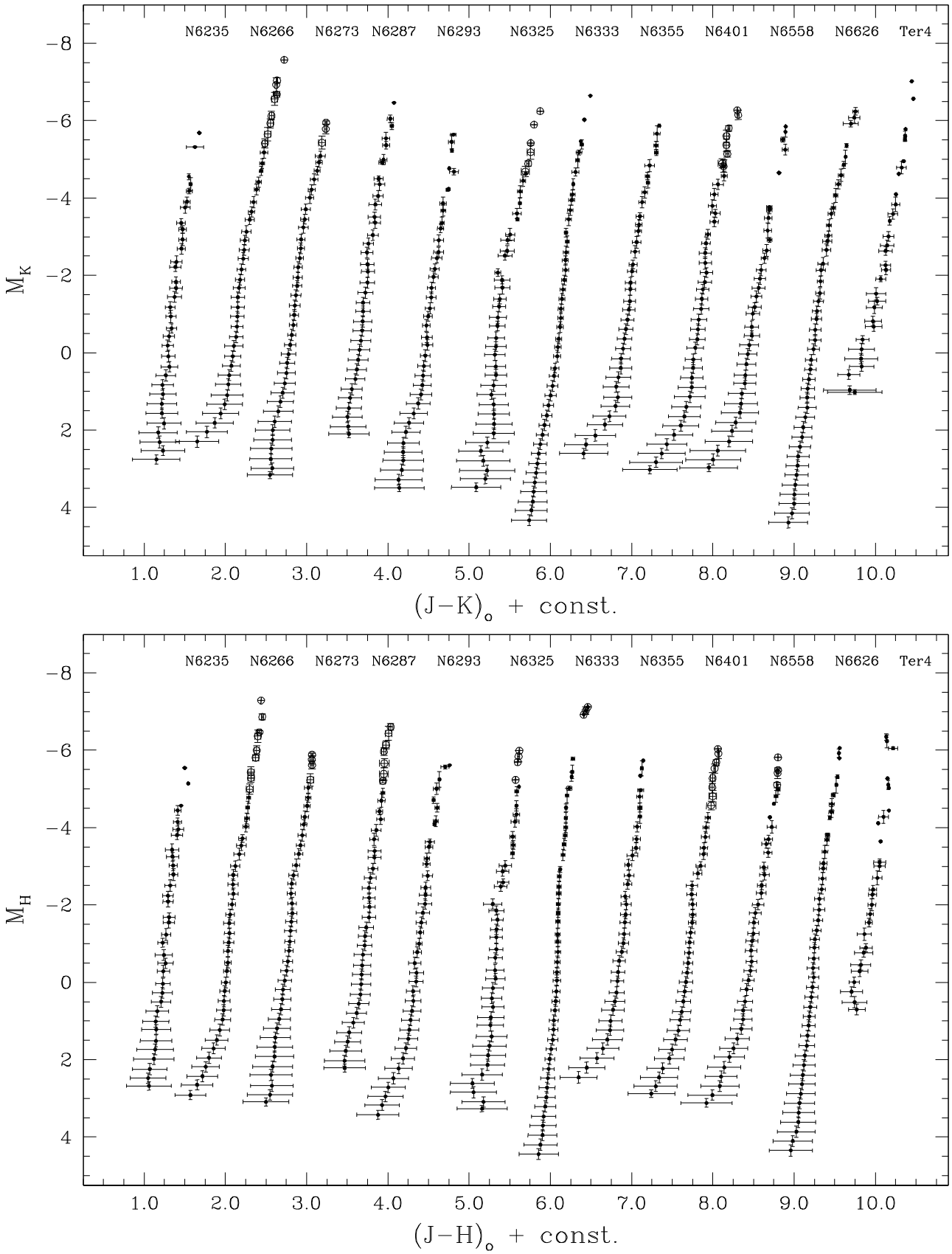

Fig. 2. Fiducial normal points of target clusters in $(J-K)_o - M_K$ (*upper*) and $(J-H)_o - M_H$ (*lower*) planes. For clarity, the colors are given zero-point offsets; from left to right, these are const. = 0.8, 1.6, 2.4, 3.2, 4.0, 4.8, 5.6, 6.4, 7.2, 8.0, 8.8, and 9.6 magnitudes. Open circles indicate fiducial normal points determined from the 2MASS data.

Table 3. The RGB colors of the observed bulge clusters at different magnitudes.

Target	$(J-K)_o^{-5.5}$	$(J-K)_o^{-5}$	$(J-K)_o^{-4}$	$(J-K)_o^{-3}$	$(J-H)_o^{-5.5}$	$(J-H)_o^{-5}$	$(J-H)_o^{-4}$	$(J-H)_o^{-3}$
This paper								
NGC 6235	0.853 ± 0.04	0.794 ± 0.04	0.716 ± 0.04	0.659 ± 0.05	0.697 ± 0.05	0.676 ± 0.05	0.624 ± 0.05	0.550 ± 0.06
NGC 6266	0.908 ± 0.03	0.864 ± 0.03	0.761 ± 0.04	0.657 ± 0.06	0.737 ± 0.03	0.699 ± 0.03	0.645 ± 0.04	0.531 ± 0.06
NGC 6273	0.812 ± 0.04	0.761 ± 0.04	0.635 ± 0.05	0.543 ± 0.05	0.658 ± 0.04	0.634 ± 0.04	0.563 ± 0.04	0.482 ± 0.05
NGC 6287	0.794 ± 0.05	0.755 ± 0.05	0.677 ± 0.05	0.597 ± 0.08	0.649 ± 0.05	0.622 ± 0.05	0.571 ± 0.05	0.517 ± 0.07
NGC 6293	0.793 ± 0.02	0.766 ± 0.02	0.716 ± 0.04	0.643 ± 0.05	0.677 ± 0.03	0.608 ± 0.03	0.536 ± 0.03	0.486 ± 0.05
NGC 6325	0.962 ± 0.02	0.938 ± 0.02	0.809 ± 0.04	0.682 ± 0.05	0.788 ± 0.03	0.754 ± 0.03	0.665 ± 0.05	0.590 ± 0.06
NGC 6333	0.778 ± 0.02	0.741 ± 0.02	0.665 ± 0.03	0.611 ± 0.03	0.669 ± 0.02	0.633 ± 0.02	0.588 ± 0.02	0.527 ± 0.02
NGC 6355	0.912 ± 0.04	0.864 ± 0.04	0.748 ± 0.04	0.664 ± 0.05	0.725 ± 0.04	0.693 ± 0.04	0.642 ± 0.04	0.580 ± 0.05
NGC 6401	0.985 ± 0.04	0.935 ± 0.04	0.851 ± 0.04	0.758 ± 0.06	0.825 ± 0.03	0.790 ± 0.03	0.723 ± 0.03	0.641 ± 0.04
NGC 6558	0.876 ± 0.05	0.841 ± 0.05	0.760 ± 0.05	0.671 ± 0.05	0.802 ± 0.04	0.777 ± 0.04	0.706 ± 0.04	0.626 ± 0.04
NGC 6626	0.886 ± 0.04	0.826 ± 0.04	0.707 ± 0.04	0.618 ± 0.03	0.744 ± 0.03	0.705 ± 0.03	0.623 ± 0.03	0.564 ± 0.04
Terzan 4	0.769 ± 0.03	0.727 ± 0.03	0.650 ± 0.03	0.579 ± 0.03	0.650 ± 0.05	0.616 ± 0.05	0.547 ± 0.05	0.477 ± 0.05
Kim et al. (2006)								
NGC 6541	0.824 ± 0.02	0.789 ± 0.02	0.687 ± 0.02	0.595 ± 0.02	0.695 ± 0.02	0.663 ± 0.02	0.584 ± 0.02	0.511 ± 0.03
NGC 6642	0.924 ± 0.03	0.843 ± 0.03	0.720 ± 0.03	0.632 ± 0.04	0.816 ± 0.03	0.759 ± 0.03	0.659 ± 0.03	0.578 ± 0.04
NGC 6681	0.826 ± 0.02	0.778 ± 0.02	0.686 ± 0.02	0.628 ± 0.02	0.680 ± 0.03	0.644 ± 0.03	0.584 ± 0.03	0.537 ± 0.03
NGC 6717	0.968 ± 0.03	0.887 ± 0.03	0.777 ± 0.03	0.714 ± 0.03	0.820 ± 0.02	0.796 ± 0.02	0.727 ± 0.02	0.650 ± 0.02
NGC 6723	0.940 ± 0.02	0.899 ± 0.02	0.787 ± 0.03	0.696 ± 0.03	0.751 ± 0.03	0.717 ± 0.03	0.665 ± 0.04	0.580 ± 0.03

and the absolute magnitudes of the RGB bumps and tips. The RGB parameters for 12 clusters in this paper, which have been used with the 5 clusters in Kim et al. (2006) to examine the overall behaviors of the RGB morphology in the near-infrared CMDs as a function of cluster metallicity for the metal-poor globular clusters in the Galactic bulge direction. The results were compared with the previous observational calibrations of Valenti et al. (2004a, 2007) and the theoretical predictions of the Yonsei-Yale isochrones (Kim et al. 2002; Yi et al. 2003).

4.1. The RGB shape

To characterize the overall behaviors of the RGB morphology in the near-infrared and optical CMDs of globular clusters, Ferraro et al. (2000) defined a new set of photometric indices for the RGB location, i.e., colors at fixed magnitudes and magnitudes at fixed colors. In a similar fashion, Kim et al. (2006) measured the photometric color and magnitude indices of the RGB morphology for five metal-poor globular clusters in the bulge direction, and compared the results with calibrations of the RGB morphology for 28 bulge clusters from Valenti et al. (2004a, 2005). The representative morphological parameters of the RGB include (1) $(J-K)_o$ and $(J-H)_o$ colors at four fixed absolute magnitude levels of $M_K = M_H = (-5.5, -5, -4,$ and $-3)$, (2) the absolute magnitudes of M_K and M_H at fixed colors of $(J-K)_o = (J-H)_o = 0.7$, and (3) the slope in the $(J-K, K)$ color-magnitude plane.

In the present study, we also measured the same parameters for the observed clusters. To derive the RGB location parameters in color and in magnitude, we applied a second- or third-order polynomial fit to adjacent $\gtrsim$10 fiducial normal points of CMDs in Fig. 2 at the given magnitude and color. The RGB slope has usually been determined by fitting an equation of the form $J-K = aK + b$ to the upper part of the RGB in the $(J-K, K)$ CMD, where the RGB morphology is less curved than in the other lower faint ranges. As in Kim et al. (2006), the fiducial normal points in a magnitude range between 0 and 5 mag fainter than the brightest point were used to determine the RGB slope. Table 3 lists the determined $(J-K)_o$ and $(J-H)_o$ colors at different magnitude levels. Furthermore, the absolute magnitudes M_K at $(J-K)_o = 0.7$ and M_H at $(J-H)_o = 0.7$ and the RGB slope are presented in Table 4. In Tables 3 and 4, we also list RGB shape parameters previously studied by our group (i.e., Kim et al. 2006) for 5 metal-poor clusters in the bulge direction.

Table 4. The RGB magnitudes at different colors, and the RGB slopes for the observed bulge clusters.

Target	$M_K^{(J-K)_o=0.7}$	$M_H^{(J-H)_o=0.7}$	$RGB_{\rm slope}$
This paper			
NGC 6235	−3.55 ± 0.64	−5.56 ± 1.11	−0.068 ± 0.006
NGC 6266	−3.49 ± 0.57	−4.90 ± 0.45	−0.098 ± 0.008
NGC 6273	−4.60 ± 0.36	...	−0.084 ± 0.009
NGC 6287	−4.45 ± 1.11	−6.17 ± 0.76	−0.069 ± 0.008
NGC 6293	−4.03 ± 0.42	−5.63 ± 0.16	−0.066 ± 0.004
NGC 6325	−3.10 ± 0.51	−4.30 ± 0.35	−0.106 ± 0.010
NGC 6333	−4.55 ± 0.46	−6.06 ± 0.26	−0.064 ± 0.003
NGC 6355	−3.48 ± 0.64	−5.14 ± 0.59	−0.078 ± 0.008
NGC 6401	−2.09 ± 0.97	−3.72 ± 0.47	−0.087 ± 0.010
NGC 6558	−3.22 ± 0.58	−3.73 ± 0.63	−0.083 ± 0.004
NGC 6626	−3.93 ± 0.53	−5.01 ± 0.47	−0.095 ± 0.005
Terzan 4	−4.68 ± 0.37	−6.28 ± 0.79	−0.075 ± 0.005
Kim et al. (2006)			
NGC 6541	−4.14 ± 0.23	−5.56 ± 0.34	−0.072 ± 0.003
NGC 6642	−3.71 ± 0.28	−4.51 ± 0.37	−0.104 ± 0.006
NGC 6681	−4.10 ± 0.25	−5.94 ± 0.24	−0.075 ± 0.003
NGC 6717	−2.73 ± 0.33	−3.66 ± 0.25	−0.077 ± 0.004
NGC 6723	−3.05 ± 0.37	−4.87 ± 0.50	−0.082 ± 0.003

In Figs. 3 and 4, we present the colors at fixed magnitudes of $M_K = M_H = (-5.5, -5, -4,$ and $-3)$ as functions of cluster metallicity $[{\rm Fe/H}]_{\rm CG97}$ and global metallicity [M/H] for the samples of clusters in this paper and Kim et al. (2006). It includes the calibration relations of Valenti et al. (2004a) for globular clusters spanning a metallicity range of $-2.12 \leqslant [{\rm Fe/H}] \leqslant -0.49$ in the Galactic bulge and halo. As can be seen in Figs. 3 and 4, the trends of the RGB color indices of $(J-K)_o$ and $(J-H)_o$ as a function of metallicity agree well with the calibrations put forward by Valenti et al. (2004a). The RGB color indices of $(J-K)_o$ and $(J-H)_o$ scale linearly with the cluster metallicity because the RGB color indices are bluer for the metal-poor clusters than the metal-rich clusters. In addition, the fit slope increases progressively toward the RGB tip. Theoretical predictions of the RGB location parameters $(J-K)_o$ and $(J-H)_o$ were extracted from

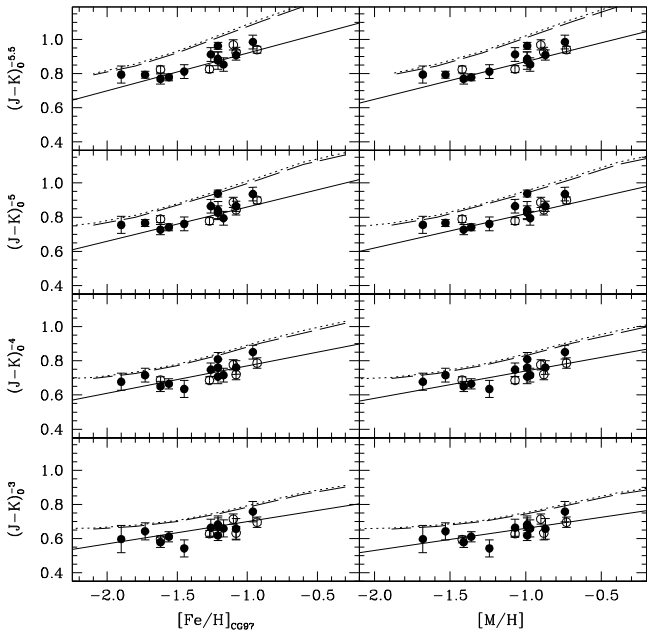

Fig. 3. RGB $(J-K)_o$ color indices at fixed magnitudes of M_K as a function of the metallicity [Fe/H]$_{CG97}$ and the global metallicity [M/H]. Filled circles and open circles represent 12 metal-poor bulge clusters observed here and 5 bulge clusters in Kim et al. (2006), respectively. Solid lines are the calibration relations of Valenti et al. (2004a). Dotted and dashed lines are the theoretical predictions of the Yonsei-Yale isochrones (Kim et al. 2002; Yi et al. 2003) at t = 12 Gyr and 10 Gyr, respectively.

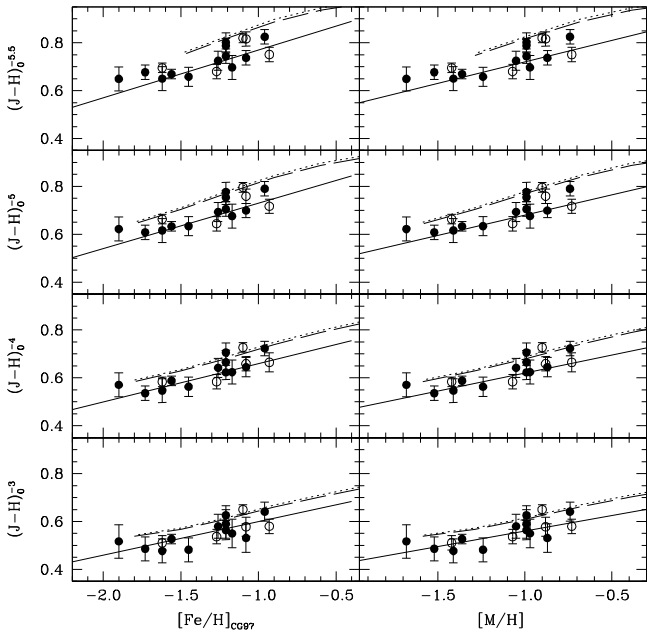

Fig. 4. RGB $(J-H)_o$ color indices at fixed magnitudes of M_H as a function of the metallicity [Fe/H]$_{CG97}$ and the global metallicity [M/H]. Symbols are the same as in Fig. 3.

the Yonsei-Yale isochrones (Kim et al. 2002; Yi et al. 2003) in order to compare them with the observed relations of the RGB colors and cluster metallicity. While the overall trends in the theoretical models show a good correlation with the observed data, it appears that there are systematic shifts in the RGB colors in our results from the relations inferred from the Yonsei-Yale isochrones. Indeed, the theoretical model colors of the RGB at [Fe/H] $= -1.5$ seem to be ∼0.06−0.11 mag redder in $(J-K)$

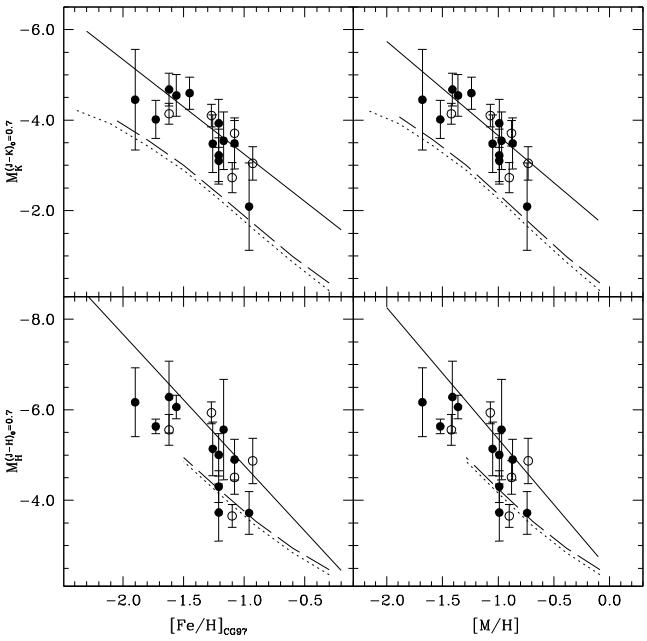

Fig. 5. RGB magnitude indices M_K and M_H at fixed color $(J-K)_o$ = $(J-H)_o$ = 0.7 as a function of the metallicity [Fe/H]$_{CG97}$ and the global metallicity [M/H]. Symbols are the same as in Fig. 3.

and ∼0.04−0.09 mag redder in $(J-H)$ than the empirical results of Valenti et al. (2004a). In addition, the shifts of the model colors become higher toward the RGB tip. The shifts can be understood as a combination of the uncertainties involved in the color calibration of log T into $(J-K)_o$ colors (Kim 2009, private communications) and in the magnitude transformation of K into the 2MASS system, the errors in the abundance determinations, and the photometric errors in the observed colors.

Figure 5 shows the dependence of the absolute magnitudes of M_K and M_H at fixed colors of $(J-K)_o = (J-H)_o = 0.7$ on the metallicity of the clusters investigated in this study. The values measured in our sample fit well with the calibration relations of Valenti et al. (2004a). We note, however, the observed clusters in this paper show a wider scattered distribution of the M_K and M_H magnitudes, than the distribution of metal-rich bulge globular clusters and halo clusters of Valenti et al. (2004a). This is possibly caused by the uncertainty in the derived absolute magnitudes associated with errors in the distance and reddening, and errors in the polynomial fitting measurements on the fiducial normal points. In fact, Valenti et al. (2004a) note that errors in color of a few hundredths of a magnitude produce uncertainties of about 0.2−0.3 in K magnitude, depending on the RGB region intercepted. On the other hand, theoretical predictions of the absolute magnitudes of M_K and M_H at fixed colors of $(J-K)_o = (J-H)_o = 0.7$ from Yonsei-Yale isochrones seem to be much fainter than the observed calibrations. The magnitude shifts of the theoretical models at [Fe/H] $= -1.5$ are ∼1.3−1.4 mag fainter in M_K and M_H than the empirical results of Valenti et al. (2004a). Here, we attribute the discrepancy to the uncertainties in the color calibration of the theoretical isochrone models.

The RGB slope is a useful parameter as it provides a photometric estimate of cluster metallicity. Indeed, the RGB slope becomes progressively flatter with increasing metallicity, mainly because the enhanced molecular blanketing could result in redder colors at a constant temperature in the coolest and brightest stars (Ortolani et al. 1991; Kuchinski et al. 1995). Moreover, the

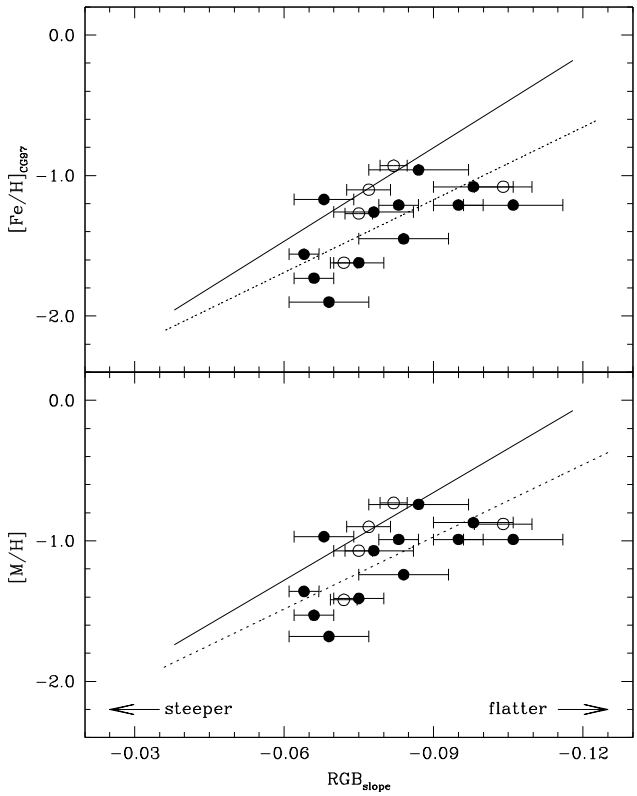

Fig. 6. The RGB slope as a function of metallicity. The dotted lines are the relations found by Ivanov & Borissova (2002). The other symbols are the same as in Fig. 3.

RGB slope in a CMD is independent of reddening and the distance of a cluster. Figure 6 shows the measured RGB slopes as a function of metallicity for the 17 program clusters with the empirical calibration relations from Valenti et al. (2004a) and the theoretical predictions from Ivanov & Borissova (2002). It is apparent in Fig. 6 that the trends for the dependency of the RGB slopes on the metallicity is consistent with previous observational calibrations and theoretical predictions; i.e., the steeper the RGB slope, the lower the metallicity of the cluster. We also find good consistency in the theoretical predictions of the distribution of the observed RGB slopes for the metal-poor bulge globular clusters. However, the estimated values of the RGB slopes for the observed metal-poor clusters tend to be flatter at a given metallicity than the corresponding values in the previous empirical calibrations of Valenti et al. (2004a) for the metal-rich bulge clusters and the halo clusters. This disagreement between our results and the relations found by Valenti et al. (2004a) is presumably from the difference in the methods used to determine the RGB slope. Indeed, Valenti et al. (2004a) fit the fiducial ridge line of the RGB in a magnitude range between 0.5 and 5 mag that is fainter than the brightest stars of each cluster, while we used the fiducial normal points in a magnitude range between 0 and 5 mag fainter than the brightest point to keep consistency with the results in Kim et al. (2006). The discrepancy might stem from the difficulty in estimating the RGB slope for the metal-poor globular clusters in $(J-K, K)$ plane, especially where the RGB is steeper than in any other plane, as mentioned in Valenti et al. (2004a). In particular, the near-infrared CMDs in the magnitude range that fits the RGB slope for a metal-poor globular cluster can be contaminated by HB stars despite statistical decontaminations from the RGB stars. This is because the HB is not horizontal at all but slanted close to the RGB in the near-infrared CMDs.

4.2. The RGB bump and tip

The RGB bump on the CMDs has a crucial astrophysical significance for the post-main-sequence evolution of low-mass stars in a globular cluster. The position of the RGB bump for a globular cluster depends on the chemical composition, the age, and other parameters controlling the internal evolution of a star. Theoretical models of stellar evolution (e.g., Thomas 1967; Iben 1968) predict that, at some level in the hydrogen-burning shell stage in the RGB after the first dredge-up in a star, the innermost penetration of the convective envelope inside star generates a discontinuity in the hydrogen distribution profile. When the advancing hydrogen burning shell passes through the generated discontinuity, a star is expected to experience an evolutionary hesitation revealed as a temporary drop in luminosity and a change in the evolutionary rate along the RGB. This yields the RGB bump on the CMDs of stars in a globular cluster.

The detection of the RGB bump has been the subject of many studies from an empirical point of view (e.g., Fusi Pecci et al. 1990; Ferraro et al. 1999; Cho & Lee 2002; Valenti et al. 2004b, 2007; Kim et al. 2006), suggesting that the combined use of the differential and integrated luminosity functions (LFs) of the RGB stars is the best way to properly detect the RGB bump. It is more difficult, however, to detect the RGB bumps in the metal-poor globular clusters than in the metal-rich ones, because there are few stars along the bright part of the RGB sequence. Indeed, as mentioned in Valenti et al. (2004b), the RGB bumps for the metal-poor clusters occur in the brightest portion of the RGB, which is a poorly populated sequence because of the high evolutionary rate of stars at the very end of the RGB. Using the near-infrared LFs of the RGB stars, Valenti et al. (2007) recently determined the RGB bumps for Galactic-bulge globular clusters with metallicities in the range of $-1.73 \leqslant$ [Fe/H] $\leqslant -0.17$, and presented new calibrations of the relation between the cluster metallicity and the brightness of the RGB bump in the K and bolometric magnitudes, which differ from those in Valenti et al. (2004b) only at the metal-rich ends.

To construct the LF of the RGB stars for the observed globular clusters in this study, we used the RGB stars selected to define the fiducial normal points of the $(J-K, K)$ CMDs for each cluster. As mentioned in Sect. 3, the RGB stars selected to estimate the fiducial normal points only include RGB samples within 2σ deviation of the mean color for a given magnitude bin, from which we properly avoided contaminations from other populations of stars, such as asymptotic giant branch star, HB stars, and foreground field stars. Considering the sample size of the RGB stars, we adjusted the size of the magnitude bins of the LFs for each cluster, which enabled us to detect the RGB bump with an appropriate measurement error. Figure 7 shows the differential LF and the logarithmic cumulative LF of the RGB stars for the observed 11 globular clusters. We defined the RGB bump at a significant peak in the differential LF with a break in slope of the logarithmic cumulative LF for the RGB stars in a cluster. For Terzan 4, the RGB bump could not be measured, as the RGB sample is not large enough to detect the bump. Magnitudes of RGB bumps for NGC 6287 and NGC 6626 are not clearly detected in the differential LFs. Instead, the clusters show breaks in the slopes of the cumulative LFs at the magnitudes that we assigned to the RGB bumps for the clusters. Applying the distance modulus and the reddening value for each cluster in Table 3, the determined K magnitudes of the RGB bumps were transformed

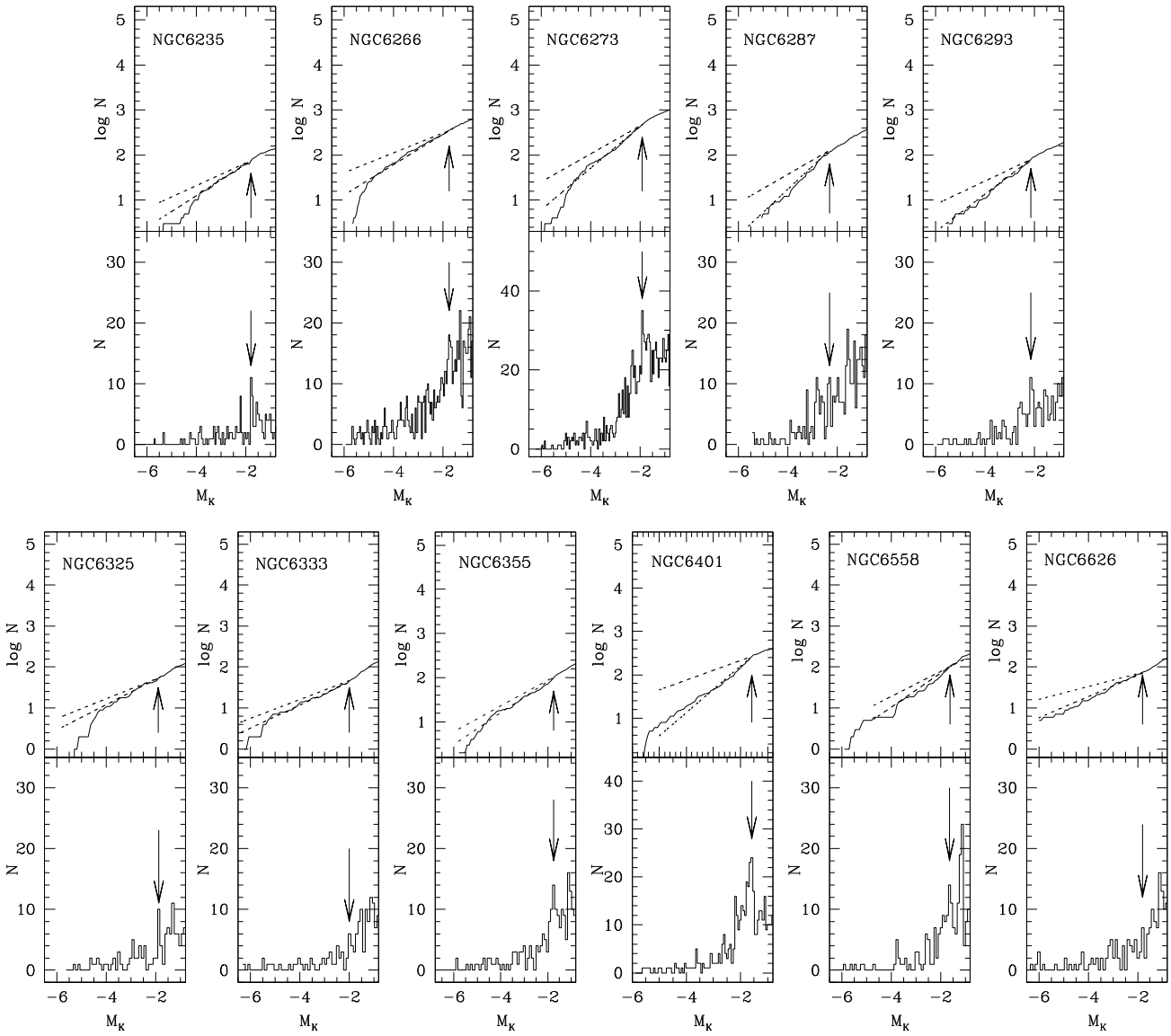

Fig. 7. The logarithmic cumulative (*upper*) and differential (*lower*) LFs for RGB stars in the observed clusters. The arrows indicate the RGB bump position. The dashed lines in the cumulative LF are the linear fit to the regions above and below the RGB bump.

into the absolute M_K magnitudes. Then, the bolometric corrections for population II giant stars provided by Montegriffo et al. (1998) were used to convert the absolute magnitudes M_K of the RGB bump into the bolometric magnitude $M_{\rm bol}$.

In Cols. (2)–(4) of Table 5, we list the observed K, the absolute M_K, and the bolometric $M_{\rm bol}$ magnitudes of the RGB bumps for the observed clusters in addition to those for 5 bulge clusters in Kim et al. (2006). The magnitude values of RGB bumps for NGC 6287 and NGC 6626, which were determined from their cumulative LFs of the RGB stars, are in parenthesis. Errors in K and M_K are measurement errors, and those in $M_{\rm bol}$ are a combination of measurement errors and the global uncertainty of the distance moduli, which is assumed to be 0.2 mag (e.g., Cho & Lee 2002). Figure 8 plots the determined M_K and $M_{\rm bol}$ of the RGB bumps versus cluster metallicity $[{\rm Fe/H}]_{\rm CG97}$ and global metallicity [M/H], indicating that the RGB bump moves to fainter locations with increasing cluster metallicity. As shown in Fig. 8, the determinations of the RGB bumps for the metal-poor clusters are consistent with the new calibrations for the Galactic bulge clusters of Valenti et al. (2007). The theoretical predictions of the RGB bump magnitudes as a function of metallicity from the Yonsei-Yale isochrones at t = 12 Gyr and 10 Gyr (Kim et al. 2002; Yi et al. 2003) show good agreement with the observations.

The RGB tip (TRGB) is the evolution along the RGB ends with helium ignition in the stellar core. Because the luminosity of the TRGB depends on the helium core mass, which is fairly constant over a large part of the low-mass star range (Salaris et al. 2002), the TRGB has a roughly constant brightness unrelated to the age of the population. Thus, the luminosity of the TRGB is widely used as a standard candle to estimate the distance to galaxies of any morphological type (e.g., Lee et al. 1993; Madore & Freedman 1995; Walker 2003). Recently, this method has also been carried out in near-infrared observations to estimate the distances of nearby galaxies and Galactic globular clusters (e.g., Montegriffo et al. 1995; Cioni et al. 2000; Cioni & Habing 2005; Bellazzini et al. 2004). In this paper, the TRGB K magnitude of the observed globular clusters were determined from the brightness measurements of the brightest RGB stars and the bright end of the observed LF of the RGB stars. However, we were able to determine the K magnitudes of the TRGBs for only 6 clusters (NGC 6273, NGC 6287,

Table 5. Magnitudes of the RGB bump and tip for the observed bulge clusters.

Target	$K^{\rm Bump}$	$M_K^{\rm Bump}$	$M_{\rm bol}^{Bump}$	$K^{\rm Tip}$	$M_K^{\rm Tip}$	$M_{\rm bol}^{\rm Tip}$
This paper						
NGC 6235	13.39 ± 0.06	−1.79 ± 0.06	0.06 ± 0.21	...	...	...
NGC 6266	12.67 ± 0.05	−1.76 ± 0.05	0.08 ± 0.21	...	...	...
NGC 6273	12.82 ± 0.05	−1.91 ± 0.05	−0.28 ± 0.21	8.78 ± 0.05	−5.96 ± 0.05	−3.43 ± 0.21
NGC 6287	(13.56 ± 0.07)	(−2.27 ± 0.07)	(−0.33 ± 0.21)	9.88 ± 0.07	−5.96 ± 0.07	−3.32 ± 0.21
NGC 6293	12.80 ± 0.08	−2.14 ± 0.08	−0.30 ± 0.22	9.28 ± 0.08	−5.66 ± 0.08	−3.25 ± 0.22
NGC 6325	12.55 ± 0.10	−1.88 ± 0.10	0.1 ± 0.22	...	...	...
NGC 6333	12.83 ± 0.10	−1.98 ± 0.10	−0.09 ± 0.22	8.82 ± 0.10	−5.99 ± 0.10	−3.53 ± 0.22
NGC 6355	13.14 ± 0.09	−1.74 ± 0.09	0.09 ± 0.22	...	...	...
NGC 6401	13.29 ± 0.06	−1.58 ± 0.06	0.55 ± 0.21	...	...	...
NGC 6558	12.83 ± 0.09	−1.63 ± 0.09	0.21 ± 0.22	...	...	...
NGC 6626	(11.96 ± 0.10)	(−1.79 ± 0.10)	(0.01 ± 0.20)	7.45 ± 0.10	−6.29 ± 0.10	−3.69 ± 0.22
Terzan 4	...	...	...	10.06 ± 0.03	−5.80 ± 0.03	−3.38 ± 0.20
Kim et al. (2006)						
NGC 6541	11.74 ± 0.09	−2.36 ± 0.09	−0.48 ± 0.22	8.59 ± 0.09	−5.67 ± 0.09	−3.22 ± 0.22
NGC 6642	13.23 ± 0.10	−1.41 ± 0.10	0.30 ± 0.22	8.29 ± 0.10	−6.35 ± 0.10	−3.53 ± 0.22
NGC 6681	13.13 ± 0.04	−1.90 ± 0.04	−0.02 ± 0.20	8.69 ± 0.04	−6.34 ± 0.04	−3.78 ± 0.20
NGC 6717	12.98 ± 0.05	−1.53 ± 0.05	0.57 ± 0.21	9.02 ± 0.05	−5.49 ± 0.05	−2.84 ± 0.21
NGC 6723	13.19 ± 0.05	−1.54 ± 0.05	0.50 ± 0.21	8.73 ± 0.05	−6.00 ± 0.05	−3.37 ± 0.21

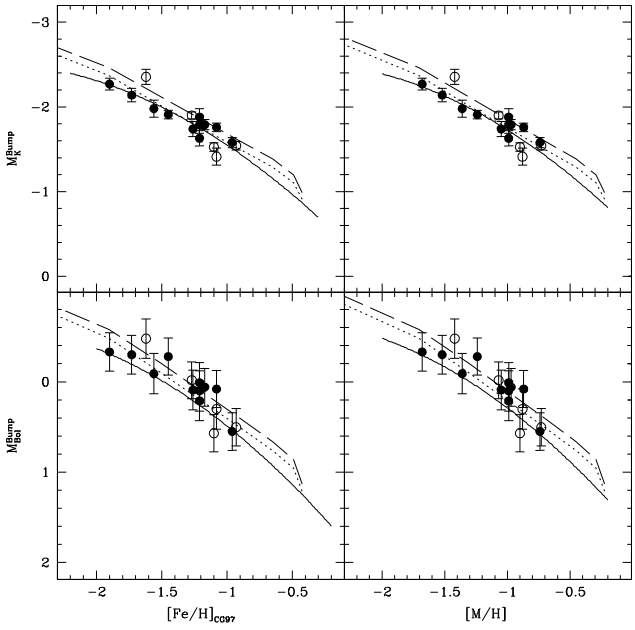

Fig. 8. The behavior of the M_K and $M_{\rm bol}$ magnitudes of the RGB bumps for the observed clusters as a function of metallicity $[Fe/H]_{CG97}$ and global metallicity [M/H]. Symbols are the same as Fig. 3.

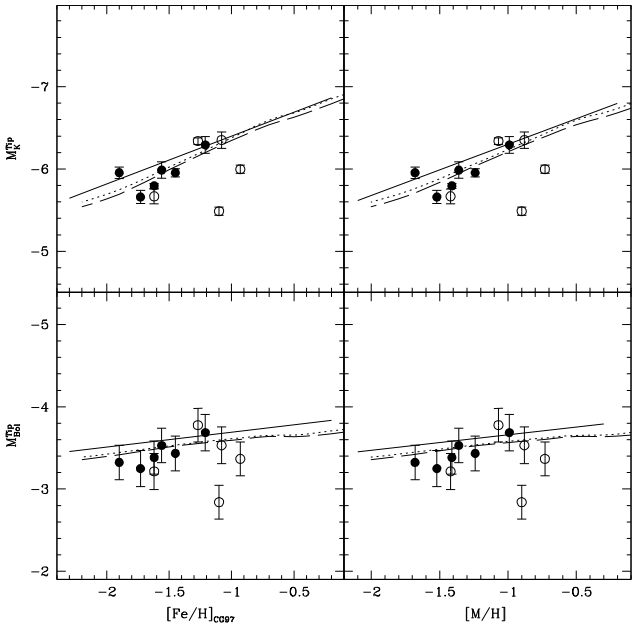

Fig. 9. The behavior of the M_K and $M_{\rm bol}$ magnitudes of the RGB tip for the observed clusters as a function of metallicity $[Fe/H]_{CG97}$ and global metallicity [M/H]. Symbols are the same as Fig. 3.

NGC 6293, NGC 6333, NGC 6626, and Terzan 4), because the brightest RGB is too poorly populated to define the TRGB in the limited area of the other observed clusters. Following the case of the RGB bumps, we estimated the absolute M_K and the bolometric $M_{\rm bol}$ magnitudes of the TRGB for the observed clusters.

The measured K, M_K, and $M_{\rm bol}$ magnitudes of the TRGB are listed in Cols. (5)–(7) of Table 5. Similar to the $M_{\rm bol}$ of the RGB bumps, errors in $M_{\rm bol}$ for the TRGB are a combination of measurement errors and the global uncertainty of 0.2 mag of the distance moduli. Figure 9 shows the relationship between the M_K and $M_{\rm bol}$ of the TRGB and the cluster metallicity of the observed 6 clusters in addition to those of the 5 clusters in Kim et al. (2006), indicating a good correlation with the previous calibrations of Valenti et al. (2004a). As noted in Kim et al. (2006), the values of the TRGB for a compact post-core-collapse cluster NGC 6717 show a significant deviation from the calibration relations, because there are still too few bright RGB stars to accurately measure the TRGB on the observed CMDs. In Fig. 9 we overlay the theoretical predictions of the TRGB magnitudes as a function of metallicity estimated from the Yonsei-Yale isochrones (Kim et al. 2002; Yi et al. 2003), and this also seems to be consistent with the observations.

5. Summary and conclusions

Detailed analyses of the RGB morphology for 12 metal-poor ([Fe/H] ≤ −1.0) globular clusters in the Galactic bulge direction were performed using high-quality, near-infrared JHK'

photometry. From the study of the RGB shapes in the near-infrared CMDs for each cluster, we measured the colors at different magnitude levels, the magnitudes at different colors, and the RGB slopes. As major RGB evolutionary features, the magnitudes of the RGB bump and tip were also determined from the LFs of the selected RGB stars in each cluster. The determined indices of the RGB morphology for the 12 observed clusters were combined with the results for 5 bulge clusters in Kim et al. (2006), so that the entire dataset comprises ~75% of the total 22 metal-poor ([Fe/H] ≤ -1.0) globular clusters within 3 kpc of the Galactic center. The behavior of the RGB morphology for the program clusters was compared with the previous empirical calibration relations as a function of cluster metallicity for the Galactic bulge globular clusters by Valenti et al. (2004a, 2007) and theoretical predictions of the Yonsei-Yale isochrones (Kim et al. 2002; Yi et al. 2003). The results are summarized as follows.

1. Photometric indices for the RGB color at fixed magnitudes, $M_K = M_H = (-5.5, -5, -4,$ and $-3)$ and the RGB magnitudes at fixed colors, $(J-K)_o = (J-H)_o = 0.7$ were measured from the fiducial normal points of the near-infrared $(J-K, K)$ and $(J-H, H)$ CMDs. Our results indicate that the correlations between the derived RGB indices and the cluster metallicity for the metal-poor globular clusters in the Galactic bulge direction are consistent with previous observational calibration relations for a sample of the metal-rich bulge clusters and the halo clusters (Valenti et al. 2004a). The theoretical models reliably represent the observed RGB color and magnitude indices, although there appears to be systematic shifts in color and magnitude, as a result of the uncertainties in the theoretical calculations and observational measurements.
2. The RGB slopes were estimated from the determined fiducial normal points at the magnitude range between 0 and 5 magnitudes fainter than the brightest point of the RGB. The distribution of the RGB slopes for the observed clusters show an expected evolutionary feature; i.e., the lower metallicity of the cluster, the steeper the RGB slope. Meanwhile, the RGB slopes for the program clusters tend to be slightly flatter than those in the previous calibrations of Valenti et al. (2004a).
3. The absolute M_K and bolometric $M_{\rm bol}$ magnitudes of the RGB bump and tip for the observed clusters were determined from the differential and cumulative LFs of the selected RGB stars. The correlations between the cluster metallicity and the derived magnitudes of the RGB bump and tip for the metal-poor clusters in the Galactic bulge direction are consistent with the recent calibration relations for the Galactic bulge clusters (Valenti et al. 2007).

Of a total of 17 metal-poor clusters presented in this paper, only two clusters-NGC 6266 and NGC 6723-have the cluster's orbital data (Dinescu et al. 1999, 2003), indicating that NGC 6723 is a halo member passing the Galactic bulge at this moment and that NGC 6266 is associated with the motion of the Galactic thick disk. Together with the derived RGB morphological properties, more information about detailed orbital data will provide more robust constraints on the role of the metal-poor globular clusters in the formation of the Galactic bulge.

Acknowledgements. This work has been supported by the Korea Research Foundation Grant funded by the Korea Government (KRF 2007-313-C00321), and also partly supported by Korea Astronomy and Space Science Institute (KASI 2009220000 and Yonsei-KASI Joint Research Program for Frontiers of Astronomy and Space Science), for which we are grateful.

References

Bellazzini, M., Ferraro, F. R., Sollima, A., Pancino, E., & Origlia, L. 2004, A&A, 424, 199
Bonatto, C., & Bica, E. 2008, A&A, 479, 741
Carreta, E., & Gratton, R. G. 1997, A&AS, 121, 95
Carpenter, J. M. 2001, AJ, 121, 2851
Carraro, G. 2005, ApJ, 621, 61
Cho, D.-H., & Lee, S.-G. 2002, AJ, 124, 977
Cioni, M.-R. L., & Habing, H. J. 2005, A&A, 429, 837
Cioni, M.-R. L, van der Marel, R. P., Loup, C., & Habing, H. J. 2000, A&A, 359, 601
Côté, P., Marzke, R. O., West, M. J., & Minniti, D. 2000, ApJ, 533, 869
Dinescu, D. I., Girard, T. M., & van Altena, W. F. 1999, AJ, 117, 1792
Dinescu, D. I., Girard, T. M., van Altena, W. F., & Lopez, C. E. 2003, AJ, 125, 1373
Ferraro, F. R., Messineo, M., Fusi Pecci, F., et al. 1999, AJ, 118, 1738
Ferraro, F. R., Montegriffo, P., Origlia, L., & Fusi Pecci, F. 2000, AJ, 119, 1282
Froebrich, D., Meusinger, H., & Scholz, A. 2007, MNRAS, 377, 54
Fusi Pecci, F., Ferraro, F. R., Crocker, D. A., Rood, R. T., & Buonanno, R. 1990, A&A, 238, 95
Harris, W. E. 1996, AJ, 112, 1487
Iben, I. Jr. 1968, Nature, 220, 143
Ivanov, V. D., & Borissova, J. 2002, A&A, 390, 937
Kim, Y.-C., Demarque, P., Yi, S. K., & Alexander, D. R. 2002, ApJS, 143, 499
Kim, J.-W., Kang, A., Rhee, J., et al. 2006, A&A, 459, 499
Kobulnicky, H. A., Monson, A. J., Buckalew, B. A., et al. 2005, AJ, 129, 239
Kuchinski, L. E., Frogel, J. A., Terndrup, D. M., & Persson, S. E. 1995, AJ, 109, 1131
Lee, M. G., Freedman, W. L., & Madore, B. F. 1993, ApJ, 417, 553
Lee, Y.-W., Demarque, P., & Zinn, R. 1994, ApJ, 423, 248
Madore, B. F., & Freedman, W. L. 1995, AJ, 109, 1645
McWilliam, A., & Rich, R. M. 1994, ApJS, 91, 749
Minniti, D., & Zoccali, M. 2008, IAUS, 245, 323
Montegriffo, P., Ferraro, F. R., Fusi Pecci, F., & Origlia, L. 1995, MNRAS, 276, 739
Montegriffo, P., Ferraro, F. R. Origlia, L., & Fusi Pecci, F. 1998, MNRAS, 297, 872
Nakasato, N., & Nomoto, K. 2003, ApJ, 588, 842
Origlia, L., Valenti, E., Rich, R. M., & Ferraro, F. R. 2005, MNRAS, 363, 897
Ortolani, S. 1999, Ap&SS, 265, 355
Ortolani, S., Barbuy, B., & Bica, E. 1991, A&A, 249, 31
Ortolani, S., Barbuy, B., & Bica, E. 1997, A&A, 319, 850
Piotto, G., King, I. R., Djorgovski, S. G., et al. 2002, A&A, 391, 945
Rich, R. M., Ortolani, S., & Barbuy, B. 1998, AJ, 116, 1295
Rieke, G. H., & Lebofsky, M. J. 1985, ApJ, 288, 618
Salaris, M., Chieffi, A., & Straniero, O. 1993, ApJ, 414, 580
Salaris, M., Cassisi, S., & Weiss, A. 2002, PASP, 114, 375
Schlegel, D. J., Finkbeiner, D. P., & Davis, M. 1998, ApJ, 500, 525
Stephens, A. W., & Frogel, J. A. 2004, AJ, 127, 925
Stetson, P. B. 1987, PASP, 99, 191
Stetson, P. B., & Harris, W. E. 1988, AJ, 96, 909
Thomas, H.-C. 1967, Z.Astrophys, 67, 420
Valenti, E., Ferraro, F. R., & Origlia, L. 2004a, MNRAS, 351, 1204
Valenti, E., Ferraro, F. R., & Origlia, L. 2004b, MNRAS, 354, 815
Valenti, E., Ferraro, F. R., Perina, S., & Origlia, L. 2004c, A&A, 419, 139
Valenti, E., Origlia, L., & Ferraro, F. R. 2005, MNRAS, 361, 272
Valenti, E., Ferraro, F. R., & Origlia, L. 2007, AJ, 133, 1287
Valenti, E., Ferraro, F. R., & Origlia, L. 2010, MNRAS, 402, 1729
Walker, A. R. 2003, in Stellar candles for the extragalactic distance scale, ed. D. Alloin, & W. Gieren (Springer), Lect. Notes Phys., 635, 265
Willman, B., Blanton, M. R., West, A. A., et al. 2005, AJ, 129, 2692
Yi, S., Demarque, P., & Kim, Y.-C. 1997, ApJ, 482, 677
Yi, S. K., Kim, Y.-C., & Demarque, P. 2003, ApJS, 144, 259
Zinn, R. J. 1985, ApJ, 293, 424
Zoccali, M., Renzini, A., Ortolani, S., et al. 2003, A&A, 399, 931